A Novel Seven-Level Active Neutral-Point-Clamped Converter With Reduced Active Switching Devices and DC-Link Voltage

Yam P. Siwakoti, *Senior Member, IEEE*, Akshay Mahajan, Daniel J. Rogers, *Member, IEEE*, and Frede Blaabjerg, *Fellow, IEEE*

***Abstract*—This paper presents a novel seven-level inverter topology for medium-voltage high-power applications. It consists of eight active switches and two inner flying capacitor (FC) units forming a similar structure as in a conventional active neutral-point-clamped (ANPC) inverter. This unique arrangement reduces the number of active and passive components. A simple modulation technique reduces cost and complexity in the control system design without compromising reactive power capability. In addition, compared to major conventional seven-level inverter topologies, such as the neutral point clamped, FC, cascaded H-bridge, and ANPC topologies, the new topology reduces the dc-link voltage requirement by 50%. This recued dc-link voltage makes the new topology appealing for various industrial applications. Experimental results from a 2.2-kVA prototype are presented to support the theoretical analysis presented in this paper. The prototype demonstrates a conversion efficiency of around 97.2% $\pm$ 1% for a wide load range.**

***Index Terms*—Active neutral-point-clamped (ANPC) inverter, flying capacitor (FC), multilevel inverter, seven-level (7L) inverter, voltage-source converter.**

I. Introduction

In RECENT years, multilevel converters have received increasing attention from both academia and industry for applications ranging from medium- to high-voltage/power conversion (e.g., >3 kV and >100 kW). This is because multilevel converters exhibit some significant advantages compared to two-level voltage-source inverters, such as improved output waveforms with lower harmonic distortion, lower electromagnetic interference, reduced stress across the semiconductor devices, and fault-tolerant operation. They are also potentially attractive for low voltage/power applications (e.g., 380 V and <100 kW) due to reduced filter size, lower switching loss, and better power quality [1]. In addition, they exhibit a favorable behavior for grid-connected renewable systems, especially for solar photovoltaic (PV) because the solid connection between the PV module and the grid via the neutral point of active neutral-point-clamped (NPC) or active neutral-point-clamped (ANPC) topologies helps us to keep the common-mode voltage constant, which reduces the leakage current in the system. This behavior is equally appealing for motor drives and marine power supply [2].

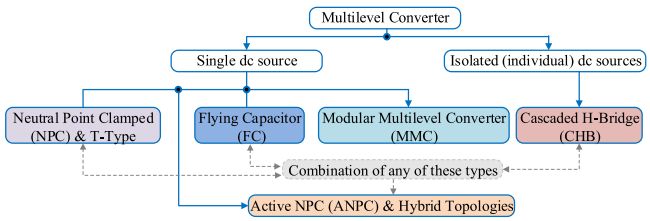

Fig. 1. Broad categorization of multilevel converter topologies.

Multilevel converter topologies have been reported in the literature since 1970s, yet there are still new topologies being investigated and finding applications in emerging areas [3]–[8]. A broad categorization of the multilevel converters is illustrated in Fig. 1. Some of the popular multilevel topologies include the NPC converter [4], [6], [10], [12]; flying capacitor (FC) converter [8], [11], [13]; cascaded H-bridge (CHB) converter [3]–[5], [20]; T-type converter [1], [5]; modular multilevel converter (MMC) [5], [16]; and hybrid multilevel NPC converter [8], [9], [12], [14]. A single-phase circuit of some of the common topologies generating a seven-level (7L) output is shown in Fig. 2. The NPC converter is easy to control with simple pulsewidth modulation (PWM) techniques; however, in many cases, the unsymmetrical loading of power devices causes underutilization [19], [21]. In addition, as the number of output voltage levels increases, the dc-link capacitor voltage balancing becomes difficult, often demanding complex control strategies [5], [15]. The FC converter is controlled by multi-carrier phase-shifted PWM and shows a symmetrical loading of power devices and spreads losses equally across the power devices [11], [18], [20]. However, the increased number of capacitors in FC-type topologies with a large number of levels leads to more complex control scheme [4], [11], [13]. In contrast, the CHB can achieve a large number of levels by a straightforward

Manuscript received July 25, 2018; revised October 26, 2018 and January 8, 2019; accepted January 26, 2019. Date of publication February 4, 2019; date of current version August 29, 2019. Recommended for publication by Associate Editor Y. Xue. *(Corresponding author: Yam Prasad Siwakoti.)*

Y. P. Siwakoti is with the Faculty of Engineering and Information Technology, University of Technology Sydney, Sydney, N.S.W. 2007, Australia (e-mail:

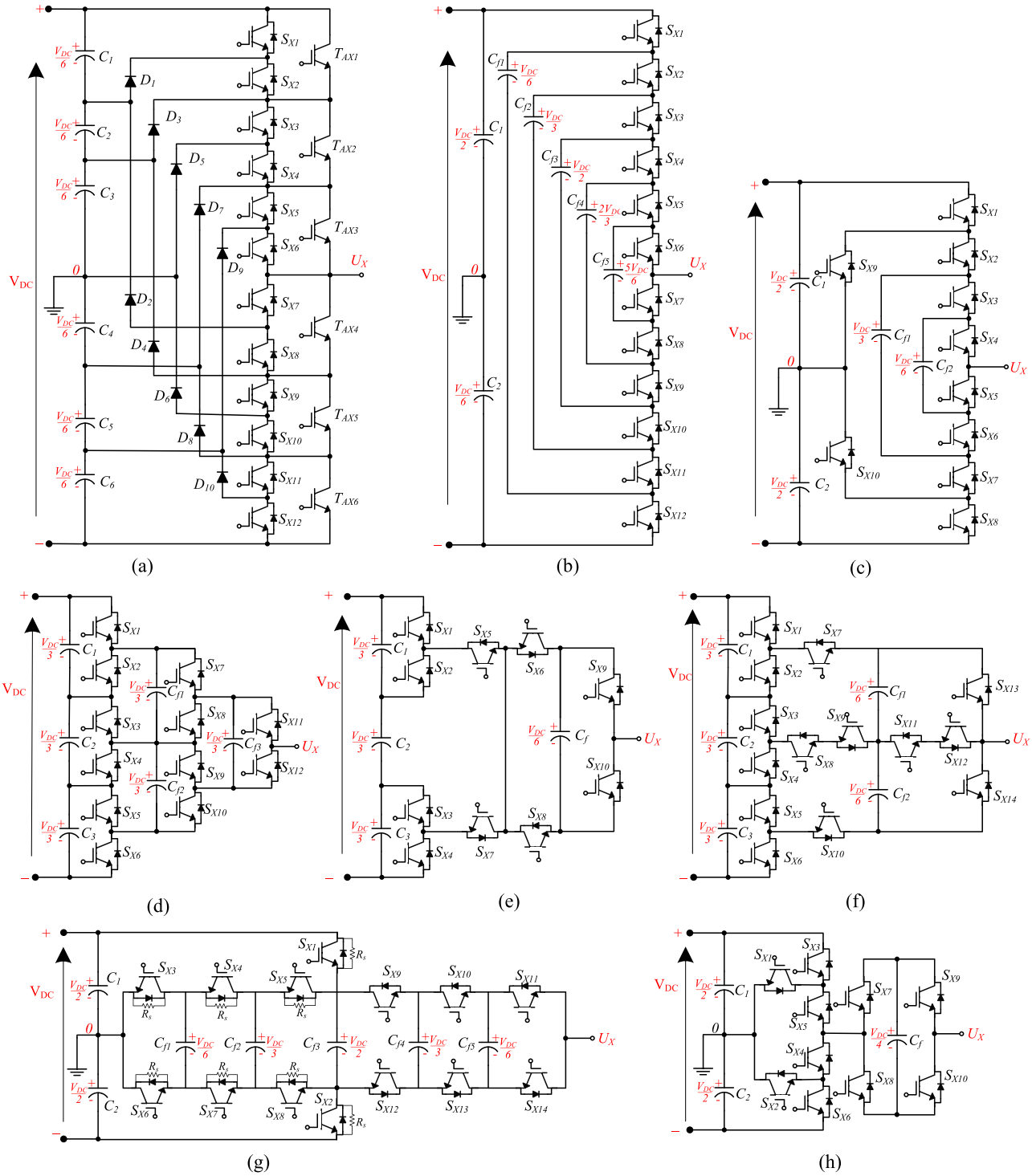

Fig. 2. Phase leg of some of the conventional 7L inverter topologies. (a) 7L-NPC [10], [19]. (b) 7L-FC [11]. (c) 7L-ANPC [12]. (d) Generalized 7L-Peng model [13]. (e) Hybrid-clamped 7L-ANPC [2]. (f) Hybrid 7L-ANPC-I [14]. (g) Hybrid 7L-ANPC-II [12]. (h) Hybrid 7L-ANPC-III [15]. Here, $X \in$ (R, Y, B) phases.

cascaded structure of H-bridges, and loss equalization can be achieved even with simple phase-shifted PWM technique. However, the CHB requires isolated dc sources for each H-bridges, potentially making the system bulky and expensive [1], [3]–[5], [16]. The T-type converter uses similar PWM strategies as the NPC topology, differing only in that one power device generates the positive or negative half of the output voltage. The power devices are loaded symmetrically in pairs but the outer power devices have to block the entire dc-link voltage during operation [1], [5]. Likewise, the increased number of capacitors in higher level FC- and MMC-type topologies leads to more complex control scheme [5], [8], [11], [13], [16].

Typically, multilevel inverters require a higher dc-link voltage which is up to two times the peak of the ac voltage

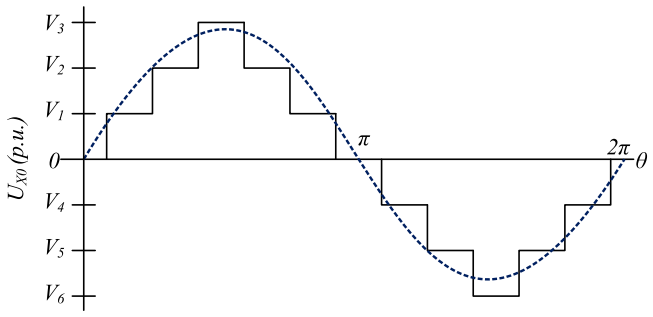

Fig. 3. Output voltage levels of different 7L inverter topologies (for $V_{\mathrm{dc-link}} = V_{\mathrm{DC}} = 1$ p.u.).

TABLE I
DIFFERENT 7L INVERTERS AND ITS OUTPUT VOLTAGE LEVELS (p.u.)

Level	Conventional				Proposed
	Mid-point clamped	Hybrid active-clamped			
	(Fig. 2 (a, b, c, g, h))	(Fig. 2 (d))	(Fig. 2 (e))	(Fig. 2 (f))	(Fig. 4 (a))
V_1	+1/6	+1/4	+1/6	+1/4	+1/4
V_2	+1/3	+1/2	+1/3	+1/2	+1/2
V_3	+1/2	+1	+1/2	+3/4	+1
V_4	-1/6	-1/4	-1/6	-1/4	-1/4
V_5	-1/3	-1/2	-1/3	-1/2	-1/2
V_6	-1/2	-1	-1/2	-3/4	-1

output. Fig. 3 and Table I summarizes the magnitude and level of the output voltage in p.u. of some of the topologies of Fig. 2 for a given dc-link voltage ($V_{\mathrm{DC}} = 1$ p.u.). It shows that dc-link voltage utilization is increased by moving from mid-point-clamped topologies [≤50% in Fig. 2(a), (b), (c), (g), and (h)] to hybrid-clamped topologies [≤75% in Fig. 2(f)]. For many applications (e.g., a grid-connected PV system), these circuits may require an additional front-end boost dc–dc converter, or string of series-connected PV modules to raise the dc-link voltage (e.g., up to 800 V for connection to a 400 V grid). Examples of the front-end dc-link supply for some of the common multilevel converters are given in Fig. 4. In general, these multi-stage power conversion approaches reduce the system efficiency and reliability, while increasing the size and cost of the system. In the case of a PV system, the additional boost stage can be eliminated by connecting PV modules in series strings to produce a higher dc-link voltage, however this potentially reduces energy yield due to mismatch between the modules (e.g., as a result of shading), which will tend to offset the improved converter efficiency. Therefore, a single-stage dc–ac power converter with boost capabilities offers an interesting alternative compared to a two-stage approach [13].

The ANPC and some hybrid topologies, which combine the concept of NPC, FC, and/or CHB have received more attention in recent times for medium-power applications as they retain most of the advantages of the parent topologies [8], [9], [12], [14], [22], and [23]. However, they still require a large number of active and passive components and a higher dc-link voltage as shown in Figs. 3 and 4. These disadvantages present a challenge in terms of developing a new power circuit which is more attractive than the classical topologies in terms of the number of components and dc-link voltage requirements. Considering this aspect, a novel eight-switch 7L-boost-ANPC inverter is investigated in this paper and discussed for general-purpose applications (e.g., rolling mills, fans, pumps, marine appliances, mining, traction, and a grid-connected renewable energy, etc.), which reduces the dc-link voltage requirement to half of the conventional multilevel inverter family, while reducing both active and passive components.

This paper is organized as follows. Section II presents the concept and analysis of the 7L-ABNPC followed by its principle of operation in Section III-A comprehensive comparison with design rules and components selection is presented in Section IV. Simulations and experimental results of the 2.2-kVA single-phase prototype are finally provided in Section V for verification, and this paper is concluded in Section VI.

II. CIRCUIT DESCRIPTION

The phase leg of the new 7L-boost-ANPC inverter consists of eight power switches and four capacitors. A schematic of the phase leg of the inverter is shown in Fig. 5(a), where $\mathrm{S_{X1}}$, $\mathrm{S_{X2}}$, …, $\mathrm{S_{X8}}$ (X ∈ (R, Y, B) phases) are the switching devices. The corresponding modulating and switching signals are shown in Fig. 5(b). Among the eight switches, two switches ($\mathrm{S_{X3}}$ and $\mathrm{S_{X8}}$) are devices with a bipolar voltage-blocking capability and unipolar controllability, e.g., a reverse-blocking IGBT (RB-IGBT) or an IGBT/MOSFET with a series diode, and the other six ($\mathrm{S_{X1}}$, $\mathrm{S_{X2}}$, $\mathrm{S_{X4}}$, $\mathrm{S_{X5}}$, $\mathrm{S_{X6}}$ and $\mathrm{S_{X7}}$) are standard reverse-conducting unipolar voltage devices, such as a MOSFET/IGBT. Similar to the conventional 7L-NPC, 7L-ANPC, and 7L-FC topologies, the dc link consists of two series-connected capacitors C_1 and C_2, whose rated voltages are half the dc-link voltage. The combination of switches $\mathrm{S_{X1}}$, $\mathrm{S_{X4}}$, and $\mathrm{S_{X5}}$ or $\mathrm{S_{X2}}$, $\mathrm{S_{X6}}$, and $\mathrm{S_{X7}}$ form bidirectional current carrying paths, which connects the ac terminal to the dc-link mid-point "0" (dc neutral point). The FC C_{F1} charges to V_{dc} through $\mathrm{S_{X3}}$ and $\mathrm{S_{X8}}$ in every switching cycle from the input supply V_{dc} to create a full-virtual dc bus for the third level ($0.5V_{\mathrm{dc}}$ to $\mathrm{V_{dc}}$ or $-0.5V_{\mathrm{dc}}$ to $-V_{\mathrm{dc}}$) in the output voltage waveform before the filter. Similarly, the FC C_{F2} charges to $0.25V_{\mathrm{dc}}$ through $\mathrm{S_{X3}}$, $\mathrm{S_{X4}}$, and $\mathrm{S_{X6}}$ in positive cycle and through $\mathrm{S_{X5}}$, $\mathrm{S_{X7}}$, and $\mathrm{S_{X8}}$ in the negative cycle to create the first and second levels (0 to $0.25V_{\mathrm{dc}}$ or 0 to $-0.25V_{\mathrm{dc}}$ and $0.25V_{\mathrm{dc}}$ to $0.5V_{\mathrm{dc}}$ or $-0.25V_{\mathrm{dc}}$ to $-0.5V_{\mathrm{dc}}$). Under ideal operation, the proposed inverter has seven output voltage levels: ± V_{dc}, ± V_{dc}/2, ± V_{dc}/4, and 0. The corresponding phase and line voltages in a three-phase configuration are illustrated in Fig. 6(a) and (b). To make further analysis and comparison, V_{dc} is defined as the dc-link voltage of the proposed 7L ABNPC, and V_{DC} is the dc-link voltage of the conventional 7L-NPC, 7L-ANPC, and 7L-FC topologies, where $V_{\mathrm{dc}} = V_{\mathrm{DC}}/2$.

Some of the prominent features of the new eight-switch 7L ANPC inverter are as follows.

1) A reduction in the number of components (both active and passive) compared to equivalent circuits. Only eight active switches are used per phase.
2) Full utilization of the dc-link voltage of the dc-link voltage compared to the traditional NPC, ANPC, and FC inverter families.

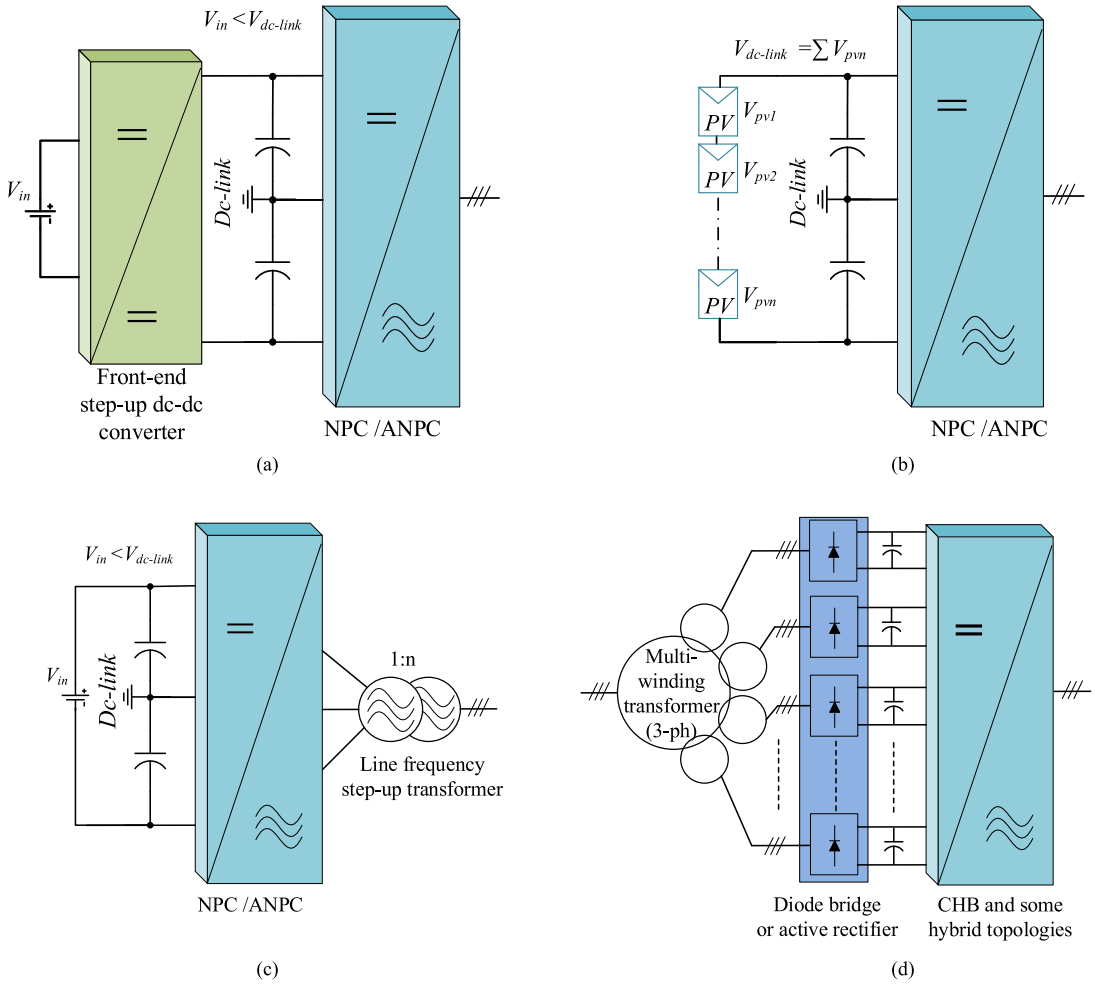

Fig. 4. Examples of front-end dc-link supply for some of the common multilevel converters. (a) Using a front-end step-up dc–dc converter, when $V_{\rm in} < V_{\rm dc-link}$. (b) Connecting PV modules in series (string), where $V_{\rm dc-link} = \sum V_{\rm PVn}$. (c) Using a line frequency step-up transformer at the output, when $V_{\rm in} < V_{\rm dc-link}$. (d) Using a multi-winding transformer and diode bridge (multi-pulse) or active rectifier for CHB (isolated) and some hybrid topologies (isolated or non-isolated).

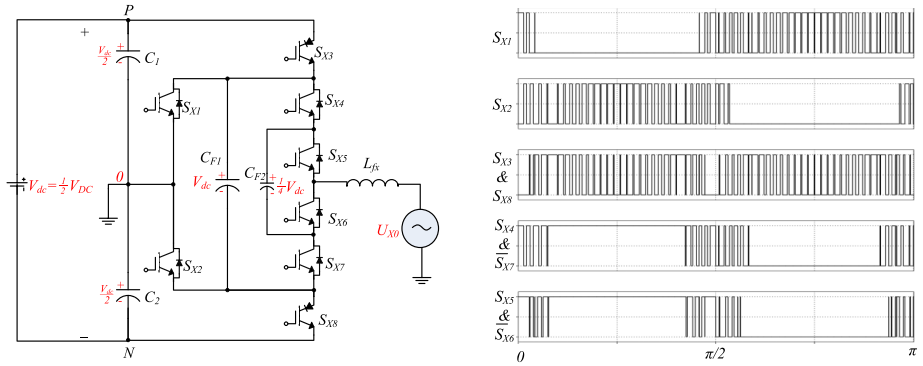

Fig. 5. Phase leg of the proposed 7L-boost-ANPC inverter with gate signal for four switches. Here, X ∈ (R, Y, B) phases.

3) The voltage stress on switches is the same as the conventional NPC, ANPC, and FC inverter families, i.e., the maximum voltage stress on each switch is $V_{\rm dc} = V_{\rm DC}/2$.

4) The voltage stress on the dc-link capacitor is halved, which reduces the size and equivalent-series resistance of the capacitor.

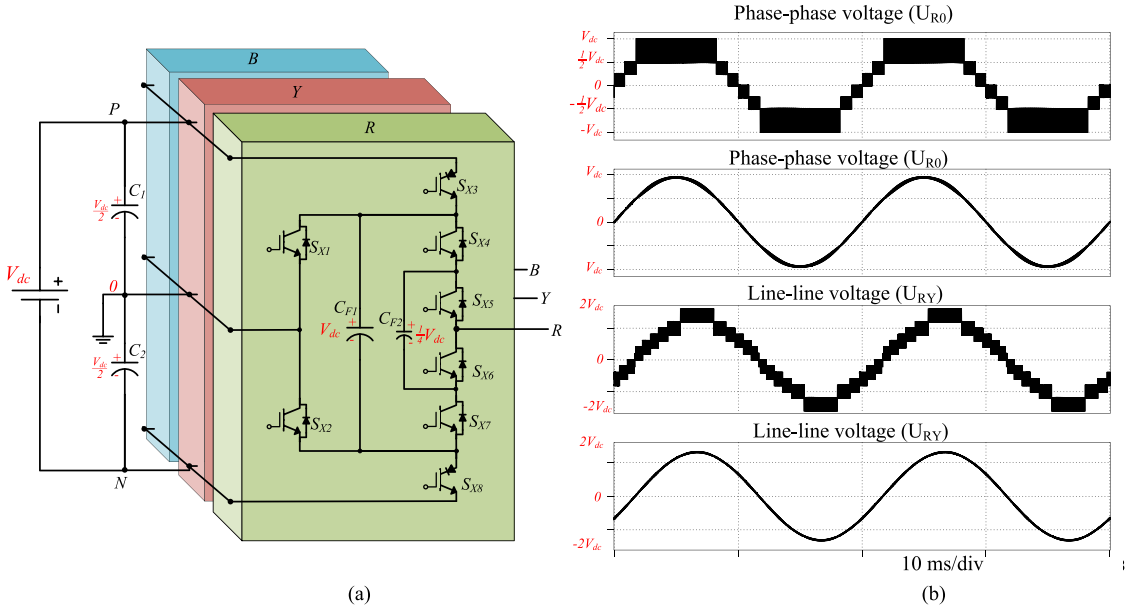

Fig. 6. Proposed 7L three-phase inverter circuit illustrating its output phase voltage (U_{R0}) and line voltage (U_{RY}).

5) The inverter can operate at any power factor (leading/lagging), which in grid applications can be used to provide reactive power support, for example.

III. Operating Modes and Modulation Strategy

A. Unity Power-Factor Operation

The operation of the inverter for positive real power flow (dc to ac) consists of ten switching states which generate the 7L voltage at the output using the capacitor voltages. Considering a dc-link voltage of $V_{\rm dc}$, each dc-link capacitor voltage is maintained at an average of $0.5\,V_{\rm dc}$, the voltage of the capacitor C_{F1} is maintained at $V_{\rm dc}$ and C_{F2} is maintained at $0.25\,V_{\rm dc}$. The active switches ($\rm S_{X1}$ and $\rm S_{X2}$) of the converter clamp to the neutral point to ensure the equal voltage sharing between the main switches ($\rm S_{X3}$–$\rm S_{X6}$) and create additional zero-voltage switching states. The converter switching states are shown in Fig. 7 (state A to J) and are accompanied by the corresponding current paths. The output voltage level, corresponding switching states, and current through C_{F1} and C_{F2} are listed in Table II. The output current is defined as i_x, and U_{xo} represents the output voltage with reference to the neutral point. Fig. 8 shows a PWM scheme for the proposed inverter in unity power-factor operation with six carriers and one reference signal that are used to generate the appropriate gating signals [level-shifted (LS)-PWM] for one phase of the inverter. The capacitor $\rm C_{F1}$ charges through the dc-link voltage in states A, D, F, and I, and discharges to the load in the remaining states. These charging and discharging states are uniformly distributed over the power cycle and can be switched at every switching cycles to maintain the capacitor $\rm C_{F1}$ voltage at $V_{\rm dc}$ [24]. Similarly, there are two pairs of redundant switching states in the ±1 and ±2 levels (states A and B in $+1$ and $+2$) and (states F and G in -1 and -2), which have an equal and opposite impact on $C_{\rm FC2}$ voltage. The effect of redundant switching states in both ±1 and ±2 levels on the C_{F2} voltage is opposite. As a result, the regulation of C_{F2} voltage in both levels can be achieved by proper selection of redundant switching states. To keep the voltage of C_{F2} balanced, the sign of the output current i_x and the actual value of C_{F2} voltage can be used to decide which redundant switching state to select.

TABLE II
Switching States of the Proposed 7L Inverter

Switching States	Level	Output Voltage (U_{xo})	S_{X1}	S_{X2}	S_{X3}	S_{X4}	S_{X5}	S_{X6}	S_{X7}	S_{X8}	i_{CF1}	i_{CF2}	*Impact to V_{CF1}*	*Impact to V_{CF2}*
A	2	+¼V_{dc}	0	0	1	1	0	1	0	1	i_{cf}	i_x	↑	↑
B		+¼V_{dc}	0	1	0	0	1	0	1	0	0	$-i_x$	–	↓
C	1	0	1	0	0	1	1	0	0	0	0	0	–	–
D	3	+½V_{dc}	0	0	1	1	1	0	0	0	i_{cf}	0	↑	–
E	4	+V_{dc}	0	1	0	1	1	0	0	0	i_x	0	↓	–
F	5	-¼V_{dc}	0	0	1	0	1	0	1	1	i_{cf}	i_x	↑	↑
G		-¼V_{dc}	1	0	0	1	0	1	0	0	0	$-i_x$	–	↓
H	1	0	0	1	0	0	0	1	1	0	0	0	–	–
I	6	-½V_{dc}	0	0	1	0	0	1	1	1	i_{cf}	0	↑	–
J	7	-V_{dc}	1	0	0	0	0	1	1	0	$-i_x$	0	↓	–

Note: "–" means no impact; "↓" means decrease; and "↑" means increase.

From Fig. 8, the modulation index M is defined as

$$M = \frac{V_{\rm ref,max}}{4A_c} \tag{1}$$

where $V_{\rm ref,max}$ is the maximum amplitude value of the reference waveform $V_{\rm ref} = 4A_c\sin(2\pi f_{\rm ref}t)$ and A_c is the amplitude of the carrier waveform. At $t = t_1$, $V_{\rm ref} = A_c$ and $t = t_2$, $V_{\rm ref} = 2A_c$. Using this, times t_1 and t_2 and corresponding angles θ_1 and θ_2 can be calculated as

$$t_1 = \frac{\sin^{-1}\left(\frac{1}{4}\right)}{2\pi f_{\rm ref}} \;\Leftrightarrow\; \theta_1 = \sin^{-1}\left(\frac{1}{4}\right) \tag{2}$$

$$t_2 = \frac{\sin^{-1}\left(\frac{1}{2}\right)}{2\pi f_{\rm ref}} \;\Leftrightarrow\; \theta_2 = \frac{\pi}{6} \tag{3}$$

where $f_{\rm ref}$ is the frequency of the reference waveform.

Using (2) and (3), θ_3, θ_4, …, θ_9 can also be calculated, as $\theta_3 = \pi - \theta_2$, $\theta_4 = \pi - \theta_1$, $\theta_6 = \pi + \theta_1$, $\theta_7 = \pi + \theta_2$,

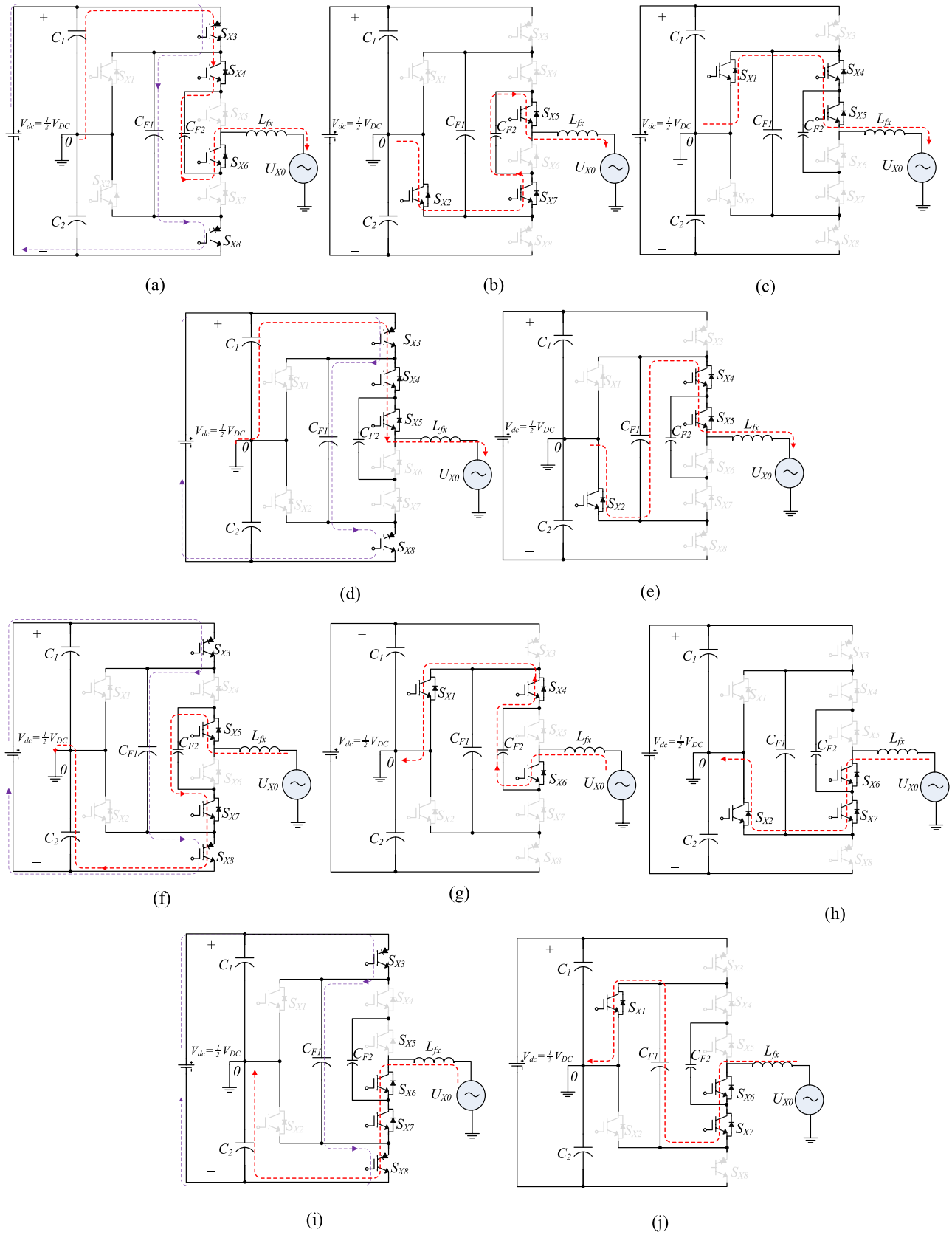

Fig. 7. Ten switching states for the 7L-ABNPC inverter. (a) State A: +1. (b) State B: +1. (c) State C: 0. (d) State D: +2. (e) State E: +3. (f) State F: −1. (g) State G: −1. (h) State H: 0. (i) State I: −2. (j) State J: −3 (red dotted-line represents the active current path, and violet dotted-line represents C_{F1} charging current path).

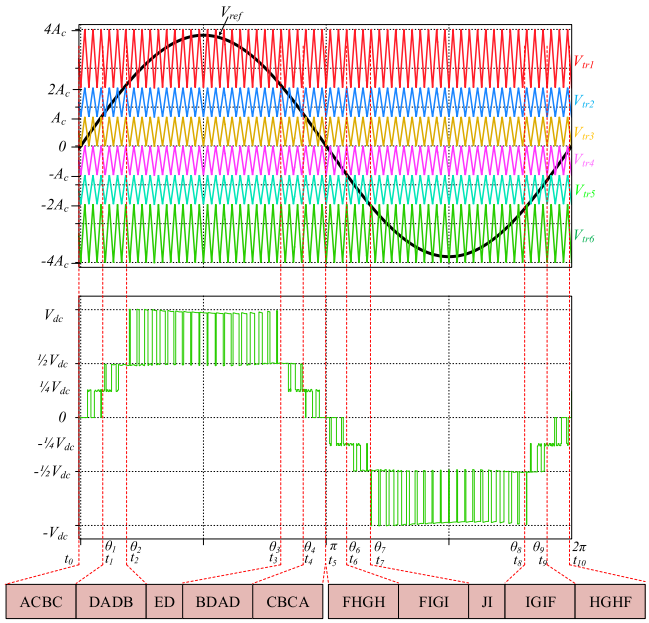

Fig. 8. LS-PWM of the 7L-ABNPC inverter showing voltage level and corresponding switching states.

$\theta_8 = 2\pi - \theta_2$, $\theta_9 = 2\pi - \theta_1$ from which $t_3, t_4, \ldots, t_{10}$ can be calculated as and when necessary.

Using the above conduction time and angle, switching pattern for each voltage level is discussed in details as below:

1) Level $+\boldsymbol{V_{dc}}/4$ $[\boldsymbol{t_0 \le t \le t_1}$ *and* $\boldsymbol{t_4 \le t \le t_5}$ *or* $\boldsymbol{0 \le \theta \le \theta_1}$ *and* $\boldsymbol{\theta_4 \le \theta \le \pi}]$*:* To keep the voltage of C_{F2} at $+V_{\rm dc}/4$ in the $+1$ level, switching states ACBC$\ldots$ from $t_0 \le t \le t_1$, and switching states CBCA$\ldots$ from $t_4 \le t \le t_5$ are used. When the output current is positive and the measured voltage of C_{F2} is lower than its reference value, then states B and F are chosen to charge C_{F2}. In this way, the C_{F2} voltage can be balanced at the reference value. The redundant switching states helps us to balance the C_{F2}, while clamping the C_{F2} to $V_{\rm dc}$ for the next higher voltage level (level $+2$).

In level $+1$, the constituent of the phase voltage (U_{X0}) can be expressed as

$$U_{X0} = \begin{cases} V_{C1} - V_{CF2} = \frac{1}{2}V_{\rm dc} - \frac{1}{4}V_{\rm dc} = +\frac{1}{4}V_{\rm dc}, & \text{State A} \\ 0, & \text{State C} \\ V_{CF2} = +\frac{1}{4}V_{\rm dc}, & \text{State B} \end{cases} \tag{4}$$

2) Level $+\boldsymbol{V_{dc}}/2$ $[\boldsymbol{t_1 \le t \le t_2}$ *and* $\boldsymbol{t_3 \le t \le t_4}$ *or* $\boldsymbol{\theta_1 \le \theta \le \theta_2}$ *and* $\boldsymbol{\theta_3 \le \theta \le \theta_4}]$*:* Similarly in level $+V_{\rm dc}/2$ from $t_1 \le t \le t_2$ and $t_3 \le t \le t_4$, the voltage across C_{F2} is maintained constant by appropriately choosing the redundant states A and B in combination with switching state D. Hence, switching states DADB$\ldots$ and BDAD$\ldots$ maintains the voltage of C_{F2} at $+V_{\rm dc}/4$, while producing the $+2$ level at the output. The continuation of state A in every alternate switching cycle also helps us to clamp the capacitor C_{F1} to $V_{\rm dc}$ for the next higher voltage level (level $+3$).

In level $+2$, the constituent of the phase voltage (U_{X0}) can be expressed as

$$U_{X0} = \begin{cases} V_{C1} - V_{CF2} = \frac{1}{2}V_{\rm dc} - \frac{1}{4}V_{\rm dc} = +\frac{1}{4}V_{\rm dc}, & \text{State A} \\ V_{C1} = +\frac{1}{2}V_{\rm dc}, & \text{State D} \\ V_{CF2} = +\frac{1}{4}V_{\rm dc}, & \text{State B} \end{cases} \tag{5}$$

3) Level $+\boldsymbol{V_{dc}}$ $[\boldsymbol{t_2 \le t \le t_3}$ *or* $\boldsymbol{\theta_2 \le \theta \le \theta_3}]$*:* Voltage level $+3$ $(+V_{\rm dc})$ from $t_2 \le t \le t_3$ can be generated by appropriately switching states E and D. In every switching cycle, the C_{F1} is clamped to the dc-link voltage, which keeps the phase voltage $U_{X0} = U_{X0,\max} = +V_{\rm dc}$. The range of the voltage fluctuation in C_{F1} in level ± 3 is determined by its capacitance, charging/discharging period, and load (magnitude and type of the load). Considering these factors in design (see Section IV-B), the voltage ripples on the capacitor should be limited to $\le 10\%$ of the V_{CF1}.

In level $+3$, the constituent of the phase voltage (U_{X0}) can be expressed as

$$U_{X0} = \begin{cases} V_{C1} = +\frac{1}{2}V_{\rm dc}, & \text{State D} \\ V_{CF1} = +V_{\rm dc}, & \text{State E.} \end{cases} \tag{6}$$

4) Level $-\boldsymbol{V_{dc}}/4$ $[\boldsymbol{t_5 \le t \le t_6}$ *and* $\boldsymbol{t_9 \le t \le t_{10}}$ *or* $\boldsymbol{\pi \le \theta \le \theta_6}$ *and* $\boldsymbol{\theta_9 \le \theta \le 2\pi}]$*:* Similar to level $+1$, the voltage across C_{F2} is maintained at $+V_{\boldsymbol{dc}}/4$ in -1 level using the redundant switching states F and G. Hence, switching states FHGH$\ldots$ from $t_5 \le t \le t_6$, and switching states HGHF$\ldots$ from $t_9 \le t \le t_{10}$ appropriately balance the voltage of C_{F2} at the reference level.

In level -1, the constituent of the phase voltage (U_{X0}) can be expressed as

$$U_{X0} = \begin{cases} -V_{C2} + V_{CF2} = -\frac{1}{2}V_{\rm dc} + \frac{1}{4}V_{\rm dc} = -\frac{1}{4}V_{\rm dc}, & \text{State F} \\ 0 = +\frac{1}{2}V_{\rm dc}, & \text{State H} \\ -V_{CF2} = -\frac{1}{4}V_{\rm dc}, & \text{State G.} \end{cases} \tag{7}$$

5) Level $-\boldsymbol{V_{dc}}/2$ $[\boldsymbol{t_6 \le t \le t_7}$ *and* $\boldsymbol{t_8 \le t \le t_9}$ *or* $\boldsymbol{\theta_6 \le \theta \le \theta_7}$ *and* $\boldsymbol{\theta_8 \le \theta \le \theta_9}]$ *:* The switching states FIGI$\ldots$ from $t_6 \le t \le t_7$ and IGIF$\ldots$ from $t_8 \le t \le t_9$ maintains C_{F2} voltage at $+V_{\rm dc}/4$, while producing -2 level at the output. The continuation of state I in every alternate switching cycle also helps us to clamp C_{F1} to $V_{\rm dc}$ for the next lower voltage level (level -3).

In level -2, the constituent of the phase voltage (U_{X0}) can be expressed as

$$U_{X0} = \begin{cases} -V_{C2} + V_{CF2} = -\frac{1}{2}V_{\rm dc} + \frac{1}{4}V_{\rm dc} = -\frac{1}{4}V_{\rm dc}, & \text{State F} \\ -V_{C2} = -\frac{1}{2}V_{\rm dc} = +\frac{1}{2}V_{\rm dc}, & \text{State I} \\ -V_{CF2} = -\frac{1}{4}V_{\rm dc}, & \text{State G.} \end{cases} \tag{8}$$

6) Level $-\boldsymbol{V_{dc}}$ $[\boldsymbol{t_7 \le t \le t_8}$ *or* $\boldsymbol{\theta_7 \le \theta \le \theta_8}]$ *:* Switching states J and I from $t_7 \le t \le t_8$ are alternately switched to generate -3 level, while clamping the voltage of C_{F1} to $V_{\rm dc}$.

In level -3, the constituent of the phase voltage (U_{X0}) can be expressed as

$$U_{X0} = \begin{cases} -V_{C2} = -\frac{1}{2}V_{\rm dc}, & \text{State J} \\ -V_{CF1} = -V_{\rm dc}, & \text{State I.} \end{cases} \tag{9}$$

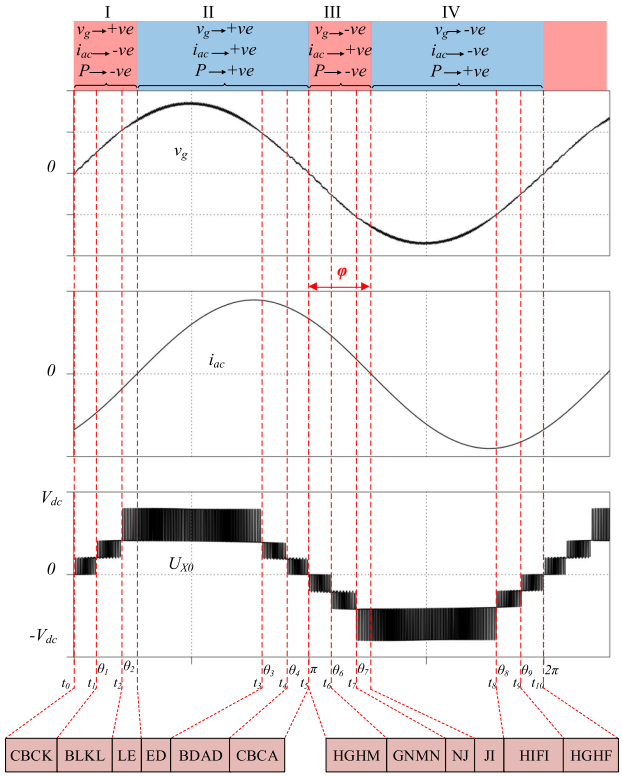

Fig. 9. Non-unity power-factor operation of the inverter illustrating its waveforms and switching pattern.

B. Non-Unity Power-Factor Operation

The operation of the inverter in the reactive mode is shown in Fig. 9, where the polarity of the output voltage and current $(v_g,\ i_{\rm ac})$ are opposite for $\varphi > \arcsin(1/2)$. Regions II and IV belong to the positive power regions (v_g and $i_{\rm ac}$ have same polarity), while regions I and III are negative power regions (v_g and $i_{\rm ac}$ have opposite polarity). The commutation of switches in the negative power region is illustrated in Fig. 10. These are not special or additional switching states on the top of the ten switching states as discussed in the unity power-factor condition (see Fig. 7), but they are natural commutation states created by the polarity and direction of the output voltage and current, respectively. A pink colored switching device indicates it is the principal current carrying device, gray colored device indicates that the device is OFF $(v_{gs} = 0)$, and blue color indicates that the device is naturally turned OFF $(v_{gs} = 1)$.

Here, $\rm S_{X3}$ and $\rm S_{X8}$ are unidirectional switches with bipolar voltage capability, but this does not limit the reactive power capability of the inverter. When v_g is positive and $i_{\rm ac}$ is negative, the current freewheels through anti-parallel diode of $\rm S_{X4}$ turning state A (+1 in Fig. 7) to state K (+1 in Fig. 10), where $\rm S_{X3}$ is naturally turned OFF by the direction of load current. The current free wheels through anti-parallel diode of $\rm S_{X4}$ and of $\rm S_{X5}$ in state L (+2 in Fig. 10), which previously flowed through the main switches ($\rm S_{X4}$ and $\rm S_{X5}$) in state D (+2 in Fig. 7). Similarly, state F and state I transform to state M and state N, respectively, when v_g is negative and $i_{\rm ac}$ is positive. Irrespective of polarity of v_g and $i_{\rm ac}$, switches $\rm S_{X1}$, $\rm S_{X4}$, and $\rm S_{X5}$ or $\rm S_{X2}$, $\rm S_{X6}$, and $\rm S_{X7}$ form a bidirectional current path during the zero-voltage state, which is common in both unity power factor and non-unity power-factor modes of operation.

During non-unity power-factor operation, the redundant commutation states with respective phase voltage (U_{X0}) can be expressed as

$$U_{X0} = \begin{cases} -V_{C2} + V_{CF1} - V_{CF2} = -\frac{1}{2}V_{\rm dc} + V_{\rm dc} - \frac{1}{4}V_{\rm dc} \\ \qquad = +\frac{1}{4}V_{\rm dc}, \quad \text{State K} \\ -V_{C2} + V_{CF1} = -\frac{1}{2}V_{\rm dc} + V_{\rm dc} = +\frac{1}{2}V_{\rm dc}, \quad \text{State L} \\ V_{C1} - V_{CF1} + V_{CF2} = \frac{1}{2}V_{\rm dc} - V_{\rm dc} + \frac{1}{4}V_{\rm dc} \\ \qquad = -\frac{1}{4}V_{\rm dc}, \quad \text{State M} \\ V_{C1} - V_{CF1} = \frac{1}{2}V_{\rm dc} - V_{\rm dc} = -\frac{1}{2}V_{\rm dc}, \quad \text{State N.} \end{cases} \tag{10}$$

The overall operation of the inverter in both unity and non-unity power-factor conditions is illustrated in Fig. 11. From this, it can be concluded that the inverter has a full reactive power capability without any special considerations, such as special modulation techniques or switch arrangements for non-unity power-factor operation.

IV. Comparative Summary and Design Guidelines

A. Comparison With Different Conventional Topologies

A comparative summary of the some of the key features of the proposed 7L inverter with the conventional 7L topologies is presented in Table III. The parameters and numbers of components included are for one-phase leg only. The total semiconductor count includes all diodes (antiparallel and/or series), MOSFETs, and IGBTs in the topology. For example, the total semiconductor count in the proposed topology is 18, which includes two RB-IGBTs or two MOSFETs with series diode (two IGBTs plus two body diodes or two MOSFETs plus two series diodes and two body diodes) plus six MOSFETs (six MOSFETs plus six anti-parallel diodes). The reduction in number of active switches to eight and the dc-link voltage requirement by 50% in the proposed 7L-ABNPC is the notable contribution compared to traditional NPC, ANPC, and FC inverter family. In addition, it does not require any additional power circuitry, i.e., transformers, rectifiers, and/or isolated dc sources for the dc-link capacitors as used in CHB [3], [5], [7], [8], [20] and some hybrid topologies [2], [20]. Table IV presents a comparative summary of the proposed 7L inverter with the conventional 7L-inverter topologies in terms of voltage stress across major components. Here, $V_{\rm dc}$ is the dc-link voltage of the proposed 7L ANPC, and $V_{\rm DC}$ is the dc-link voltage of the conventional 7L-converter topologies, where $V_{\rm dc} = V_{\rm DC}/2$. It is evident that the voltage stress on the switch in the proposed topology is the same or less than the conventional topologies. Furthermore, the voltage stress on the dc-link capacitor is reduced by 50% compared to conventional topologies with mid-point grounding. Hence, considering the number of components and device stress, the proposed converter uses the least number of components with low-voltage stress, which comparatively reduce the overall system design cost.

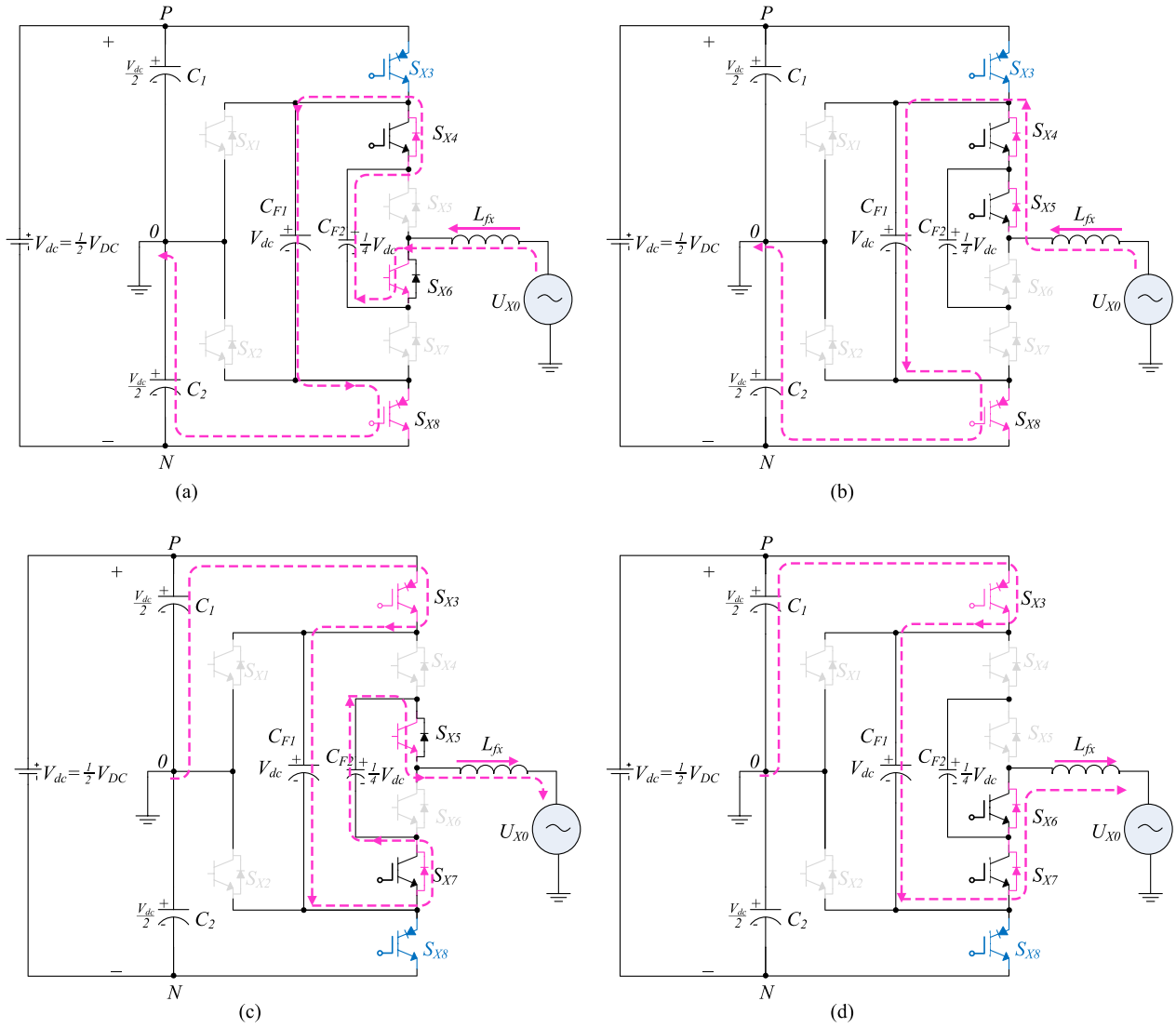

Fig. 10. Commutating states of inverter in non-unity power-factor operation. (a) State K. (b) State L. (c) State M. (d) State N.

TABLE III
COMPARATIVE SUMMARY OF THE PROPOSED 7L-BOOST ANPC WITH THE CONVENTIONAL 7L-INVERTER TOPOLOGIES (PER PHASE) IN TERMS OF NUMBER OF COMPONENTS AND DC-LINK VOLTAGE REQUIREMENTS

Parameters	Proposed	Fig. 1(a)	Fig. 1(b)	Fig. 1(c)	Fig. 1(d)	Fig. 1(e)	Fig. 1(f)	Fig. 1(g)	Fig. 1(h)
No. of Active Switches	8	18	12	10	12	10	14	14	10
No. of Capacitors	4	6	7	4	6	4	5	7	3
DC- link voltage required for the same output voltage (3-ph out)	V_{dc} =½ V_{DC}	V_{DC}	V_{DC}	V_{DC}	½ V_{DC}	V_{DC}	¾V_{DC}	V_{DC}	V_{DC}

B. Design Guidelines

The voltage and current ratings of the active switches and diodes can be deduced from Table V. However, to retain a comfortable safety margin, voltage and current ratings of the selected power devices should, therefore, be set at 150% of their theoretically calculated values.

It should also be noted that the switches in the capacitor-charging path (S_{X3} and S_{X8}) are burdened by the charging current and the load current. The charging current depends on the duty cycle $d(t)$ of the referred switch in the current path, load current $i_{ac}(t)$, and δ, where

$$d(t) = M \sin(\omega t) \tag{11}$$

$$\text{and } i_{ac}(t) = I_{ac,max} \sin(\omega t) \tag{12}$$

$$\text{and } \delta = C_{FC1}/C_{DC}. \tag{13}$$

Here, $C_{DC} = C_1 = C_2$ is the dc-link capacitance of the circuit and is calculated considering the permissible voltage

TABLE IV
SUMMARY OF VOLTAGE STRESS ON MAJOR COMPONENTS OF THE PROPOSED 7L-BOOST ANPC WITH THE CONVENTIONAL 7L-INVERTER TOPOLOGIES

Device	Fig. 1(b)	Fig. 1(c)	Fig. 1(d)	Fig. 1(e)	Fig. 1(f)	Fig. 1(g)	Fig. 1(h)	Proposed (Fig. 5(a)
S_{X1}	$\frac{1}{2}V_{DC}$	$\frac{1}{2}V_{DC}$	$\frac{1}{3}V_{DC}$	$\frac{1}{3}V_{DC}$	$\frac{1}{3}V_{DC}$	$\frac{1}{2}V_{DC}$	$\frac{1}{2}V_{DC}$	$\frac{1}{2}V_{DC}$
S_{X2}	$\frac{1}{6}V_{DC}$	$\frac{1}{6}V_{DC}$	$\frac{1}{3}V_{DC}$	$\frac{1}{3}V_{DC}$	$\frac{1}{3}V_{DC}$	$\frac{1}{2}V_{DC}$	$\frac{1}{2}V_{DC}$	$\frac{1}{2}V_{DC}$
S_{X3}	$\frac{1}{6}V_{DC}$	$\frac{1}{6}V_{DC}$	$\frac{1}{3}V_{DC}$	$\frac{1}{3}V_{DC}$	$\frac{1}{3}V_{DC}$	$\frac{1}{6}V_{DC}$	$\frac{1}{2}V_{DC}$	$\pm\frac{1}{4}V_{DC}$
S_{X4}	$\frac{1}{6}V_{DC}$	$\frac{1}{6}V_{DC}$	$\frac{1}{3}V_{DC}$	$\frac{1}{3}V_{DC}$	$\frac{1}{3}V_{DC}$	$\frac{1}{6}V_{DC}$	$\frac{1}{2}V_{DC}$	$\frac{3}{8}V_{DC}$
S_{X5}	$\frac{1}{6}V_{DC}$	$\frac{1}{6}V_{DC}$	$\frac{1}{3}V_{DC}$	$\frac{1}{3}V_{DC}$	$\frac{1}{3}V_{DC}$	$\frac{1}{6}V_{DC}$	$\frac{1}{2}V_{DC}$	$\frac{1}{8}V_{DC}$
S_{X6}	$\frac{5}{6}V_{DC}$	$\frac{1}{6}V_{DC}$	$\frac{1}{3}V_{DC}$	$\frac{1}{6}V_{DC}$	$\frac{1}{3}V_{DC}$	$\frac{1}{6}V_{DC}$	$\frac{1}{2}V_{DC}$	$\frac{1}{8}V_{DC}$
S_{X7}	$\frac{5}{6}V_{DC}$	$\frac{1}{6}V_{DC}$	$\frac{1}{3}V_{DC}$	$\frac{1}{3}V_{DC}$	$\frac{1}{6}V_{DC}$	$\frac{1}{6}V_{DC}$	$\frac{1}{4}V_{DC}$	$\frac{3}{8}V_{DC}$
S_{X8}	$\frac{1}{6}V_{DC}$	$\frac{1}{2}V_{DC}$	$\frac{1}{3}V_{DC}$	$\frac{1}{6}V_{DC}$	$\frac{1}{6}V_{DC}$	$\frac{1}{6}V_{DC}$	$\frac{1}{4}V_{DC}$	$\pm\frac{1}{4}V_{DC}$
S_{X9}	$\frac{1}{6}V_{DC}$	$\frac{1}{2}V_{DC}$	$\frac{1}{3}V_{DC}$	$\frac{1}{6}V_{DC}$	$\frac{1}{6}V_{DC}$	$\frac{1}{6}V_{DC}$	$\frac{1}{4}V_{DC}$	—
S_{X10}	$\frac{1}{6}V_{DC}$	$\frac{1}{2}V_{DC}$	$\frac{1}{3}V_{DC}$	$\frac{1}{6}V_{DC}$	$\frac{1}{6}V_{DC}$	$\frac{1}{6}V_{DC}$	$\frac{1}{4}V_{DC}$	—
S_{X11}	$\frac{1}{6}V_{DC}$	—	$\frac{1}{3}V_{DC}$	—	$\frac{1}{6}V_{DC}$	$\frac{1}{6}V_{DC}$	—	—
S_{X12}	$\frac{1}{2}V_{DC}$	—	$\frac{1}{3}V_{DC}$	—	$\frac{1}{6}V_{DC}$	$\frac{1}{6}V_{DC}$	—	—
S_{X13}	—	—	—	—	$\frac{1}{6}V_{DC}$	$\frac{1}{6}V_{DC}$	—	—
S_{X14}	—	—	—	—	$\frac{1}{6}V_{DC}$	$\frac{1}{6}V_{DC}$	—	—
C_1	$\frac{1}{2}V_{DC}$	$\frac{1}{2}V_{DC}$	$\frac{1}{3}V_{DC}$	$\frac{1}{3}V_{DC}$	$\frac{1}{3}V_{DC}$	$\frac{1}{2}V_{DC}$	$\frac{1}{2}V_{DC}$	$\frac{1}{4}V_{DC}$
C_2	$\frac{1}{2}V_{DC}$	$\frac{1}{2}V_{DC}$	$\frac{1}{3}V_{DC}$	$\frac{1}{3}V_{DC}$	$\frac{1}{3}V_{DC}$	$\frac{1}{2}V_{DC}$	$\frac{1}{2}V_{DC}$	$\frac{1}{4}V_{DC}$
C_3	—	—	$\frac{1}{3}V_{DC}$	$\frac{1}{3}V_{DC}$	$\frac{1}{3}V_{DC}$	—	—	—
C_{f1}	$\frac{1}{6}V_{DC}$	$\frac{1}{3}V_{DC}$	$\frac{1}{3}V_{DC}$	$\frac{1}{6}V_{DC}$	$\frac{1}{6}V_{DC}$	$\frac{1}{6}V_{DC}$	$\frac{1}{4}V_{DC}$	$\frac{1}{2}V_{DC}$
C_{f2}	$\frac{1}{3}V_{DC}$	$\frac{1}{3}V_{DC}$	$\frac{1}{3}V_{DC}$	—	$\frac{1}{6}V_{DC}$	$\frac{1}{3}V_{DC}$	—	$\frac{1}{8}V_{DC}$
C_{f3}	$\frac{1}{2}V_{DC}$	—	$\frac{1}{3}V_{DC}$	—	—	$\frac{1}{2}V_{DC}$	—	—
C_{f4}	$\frac{2}{3}V_{DC}$	—	—	—	—	$\frac{1}{3}V_{DC}$	—	—
C_{f5}	$\frac{5}{6}V_{DC}$	—	—	—	—	$\frac{1}{6}V_{DC}$	—	—

TABLE V
SUMMARY OF VOLTAGE AND CURRENT STRESS OF THE PROPOSED TOPOLOGY

Switches	Voltage Stress	Current Stress
S_{X1}	$+V_{dc}$	$\approx (I_{ac,max} + \Delta i_{ac})$
S_{X2}	$+V_{dc}$	$\approx (I_{ac,max} + \Delta i_{ac})$
S_{X3}	$\pm 0.5\ V_{dc}$	$\approx \left[\frac{M}{1-M}\frac{1+\delta}{1+2\delta}+1\right] I_{ac,max}$
S_{X4}	$+0.75V_{dc}$	$\approx (I_{ac,max} + \Delta i_{ac})$
S_{X5}	$+0.25V_{dc}$	$\approx (I_{ac,max} + \Delta i_{ac})$
S_{X6}	$+0.25V_{dc}$	$\approx (I_{ac,max} + \Delta i_{ac})$
S_{X7}	$+0.75V_{dc}$	$\approx (I_{ac,max} + \Delta i_{ac})$
S_{X8}	$\pm 0.5\ V_{dc}$	$\approx \left[\frac{M}{1-M}\frac{1+\delta}{1+2\delta}+1\right] I_{ac,max}$

ripple across the dc-link ($\Delta V_{\rm dc}$) as

$$C_{\rm DC,min} \geq \frac{I_{\rm dc}}{2f_s \Delta V_{\rm dc,max}}. \tag{14}$$

From (13) and (14), the minimum required $C_{\rm FC1}$ can be calculated as

$$C_{\rm FC1,min} \geq \frac{\delta V_{\rm dc}}{2f_s R_o\ \Delta V_{\rm dc,max}} \tag{15}$$

where f_s is the switching frequency, R_o is the load resistance, and $\Delta V_{\rm dc,max}$ is the allowable voltage ripple into consideration.

The current stress on $C_{\rm FC1}$ can be calculated as

$$i_{\rm FC,max} \approx \frac{M}{1-{\rm M}}\frac{1+\delta}{1+2\delta} I_{\rm ac,max} \tag{16}$$

where $I_{\rm ac,max}$ is the maximum amplitude of the load current. The charging current through S_{X3} and S_{X8} not only depends on the load, but also on M and δ. The current stress reduces with lower M and higher $C_{\rm FC}$ values. However, small ${\rm M}$ ($M < 0.8$) reduces the dc-link voltage utilization factor and large $C_{\rm FC}(\delta > 4)$ increases the cost and size of the capacitor. As a result, a compromise should be made between minimizing current stress in S_{X3} and S_{X8} and maximizing dc-link voltage utilization (which will reduce the cost and size of the FC in the circuit).

Since, the FC C_{F1} charges in both positive and negative cycles and also in both $+1$ and $+2$ levels or -1 and -2 levels. This helps us to distribute the charging current throughout the power cycle. A small inductor L_s in the range of 10 nH to 1 μH (such as coilcraft SER2000 series high-current-shielded power inductors) may also be inserted in the circuit in order to limit the current due to instantaneous voltage difference with the dc link [16]. Hence, with appropriately chosen M, δ, and $L_{\rm s}$ ($0.8 \leq {\rm M} \leq 0.95$, $1 \leq \delta \leq 4$, and $10\ {\rm nH} \leq L_s \leq 1\,\mu{\rm H}$), the current on the relevant switches in the charging current path is approximately estimated to be between $2.5I_{\rm ac,max}$ and $4I_{\rm ac,max}$. This is generally the case for most boost-type converters.

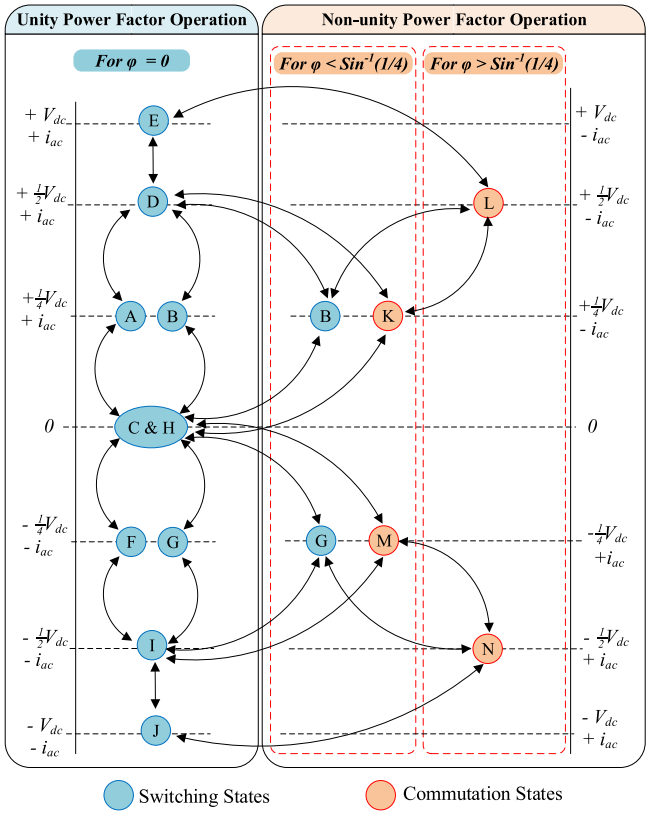

Fig. 11. Overall operation of the inverter illustrating its switching and commutation states during different power-factor angles ($\varphi = 0, \varphi < \arcsin(1/4)$, and $\varphi > \arcsin(1/4)$).

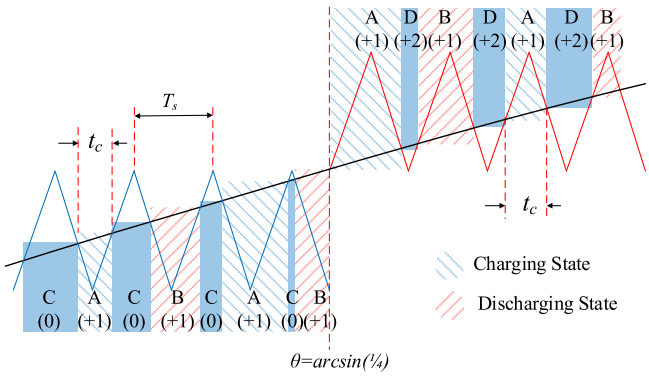

Fig. 12. Illustration of charging/discharging and control of the capacitor C_{F2} voltage.

Fig. 12 illustrates the detailed switching pattern of the inverter in $+1$ and $+2$ levels showing the charging and discharging of C_{F2}. The redundant switching states A $(+1)$ and B $(+1)$ and F (-1) and G (-1) helps us to balance the voltage of C_{F2} to $V_{\rm dc}/4$. The charging time (t_c) of C_{F2} can be written as

$$t_c = \begin{cases} = \frac{M\ \mathrm{Sin}(\theta)}{f_s/2}, & M\ \mathrm{Sin}\,(\theta) \le \frac{1}{4} \\ = \frac{1-M\ \mathrm{Sin}(\theta)}{f_s/2}, & M\ \mathrm{Sin}\,(\theta) \ge \frac{1}{4}. \end{cases} \tag{17}$$

TABLE VI
PARAMETERS AND COMPONENTS USED FOR SIMULATION AND EXPERIMENT

Description	Value/Parameter Used
Input Voltage (V_{dc})	400 V
Output voltage (v_{ac})	230 V
Power Rating (P_o)	2.2 kVA
Carrier frequency (f_s)	15 kHz
Line frequency (f)	50 Hz
dc-link capacitor (C_1 & C_2)	470 µF, 250 V
Flying capacitor (C_{FC1})	470 µF, 450 V
Flying capacitor (C_{FC2})	100 µF, 150 V
Filter inductor (L_f) & capacitor (C_f)	0.3 mH and 2.2 µF
Switches ($S_{X1} - S_{X6}$)	SCT3022AL
Diode (D_3 & D_6)	C5D50065D
Load (resistor and inductor)	2.2 kVA (30-60 Ω, 200 mH)

From (17), the voltage ripple of C_{F2} can be calculated as

$$\Delta V_{CF2} = \frac{\Delta Q_{F1}}{C_{F2}} = \frac{I_{\rm ac,max}\ \mathrm{Sin}\,(\theta)\, t_c}{C_{F1}}\ . \tag{18}$$

Using (17) and (18), this voltage ripple can be calculated in terms of $I_{\rm ac,max}$, f_s, and M as

$$\Delta V_{CF2} = \begin{cases} = \frac{I_{\rm ac,max}\ M\ \mathrm{Sin}^2(\theta)}{C_{F2} f_s/2}, & M\ \mathrm{Sin}\,(\theta) \le \frac{1}{4} \\ = \frac{I_{\rm ac,max}\left[\mathrm{Sin}(\theta) - M\ \mathrm{Sin}^2(\theta)\right]}{C_{F2} f_s/2}, & M\ \mathrm{Sin}\,(\theta) \ge \frac{1}{4}. \end{cases} \tag{19}$$

The charging time (t_c) and the capacitor voltage ripple (ΔV_{CF1}) functions are increasing from $0 \le \theta \le \arcsin(1/4)$ and are decreasing from $\arcsin(1/4) \le \theta \le \arcsin(1/2)$. The magnitude of ΔV_{CF2} reaches its maximum when $\sin(\theta) = 1/4M$. Using this condition, the minimum value of C_{F2} can be calculated as

$$C_{F2,\rm min} \ge \frac{3 I_{\rm ac,max}}{8 f_s M \Delta V_{CF2}}. \tag{20}$$

It is worth noting that the maximum voltage ripple occurs when the load is purely resistive. Once the capacitance is determined under purely resistive conditions, the voltage ripple, and, hence, the required capacitance will be smaller for a reactive load.

V. SIMULATION AND EXPERIMENTAL RESULTS

To verify the concept of the proposed inverter circuit and the theoretical analysis, several simulations using PLECS have been carried out. The parameters and component values used for both simulations and the experimental prototype are listed in Table VI. Fig. 13 shows the steady-state output voltage, load current, voltage across the FC, and the dc-link capacitors, as well as the voltage and currents occurring across/through the switches. The fifth trace in Fig. 13(a) shows an unfiltered 7L voltage, which is filtered to leave a pure fundamental-frequency sinusoidal at the load. The inverter produces an rms voltage of about 230 V for a 400-V dc-link voltage. Under unity power factor, the current and voltage are in phase. Also, it is evident that there is a natural balance in the voltage across the dc-link capacitors around its reference value $V_{C1} = V_{C2} = V_{\rm dc}/2 = 200$ V [see Fig. 13(a)]. This natural balance is maintained under different loads, modulation indexes, power factor, with different

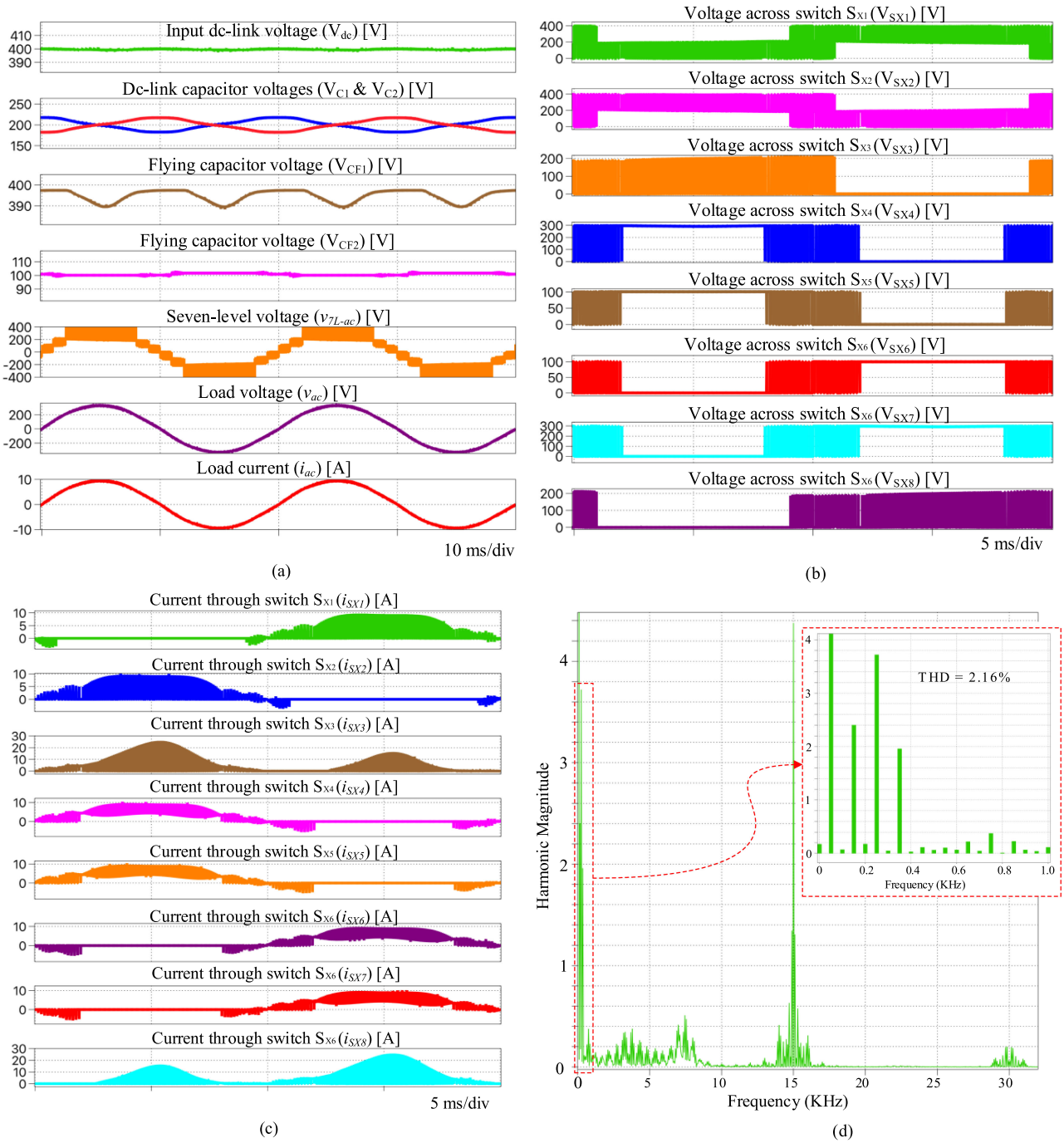

Fig. 13. Some key simulated waveforms of the proposed 7L inverter. (a) Input voltage, FCs voltages, phase voltage (with and without filter). (b) Voltage stress on switches. (c) Current stress on switches. (d) Harmonic spectrum of the output voltage.

initial capacitor voltages. As shown in Fig. 13(b) and (c), the voltage and current stress are in agreement with the analysis presented in Section IV. Fig. 13(d) shows a frequency-domain representation of the output voltage when using LS-PWM at a carrier frequency of 15 kHz. As evident, the total harmonic distortion (THD) of the output voltage and current is $<2.2\%$.

The capacity of delivering reactive power has also been successfully tested for both lagging and leading power factors. Fig. 14(a) shows the operation of the inverter in lagging power factor $\varphi_{pf} = -45°$, and Fig. 14(b) shows the operation of the inverter in leading power factor of $\varphi_{pf} = +45°$. Hence, without considering any special consideration (additional switching devices or switching sequence) or modulation technique, the inverter is capable of generating 7L output voltage; which when filtered out to get pure sinusoidal voltage and current. This verifies the seamless operation of the inverter as illustrated in Fig. 11 for any power-factor angle.

The dynamic performance of the converter under several changes in the active power is shown in Fig. 15. The converter is simulated under sudden change (step) in the load. As it can

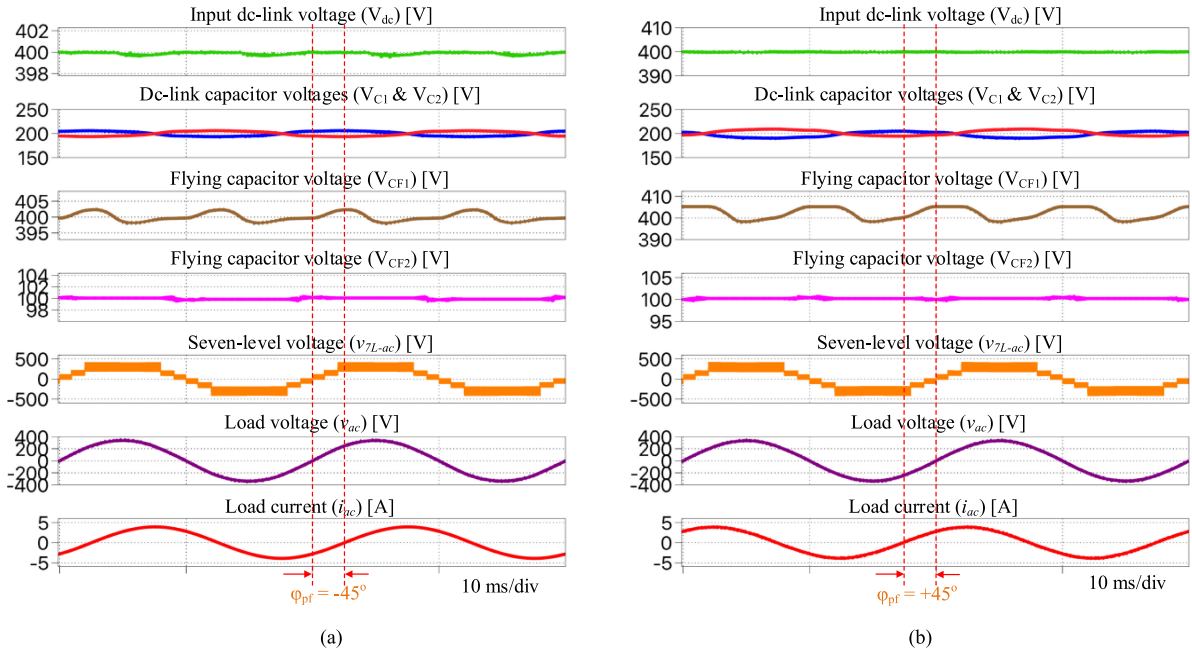

Fig. 14. Operation of the inverter during (a) lagging power factor of $\varphi_{pf} = -45°$ (*RL* load of 60 Ω + 200 mH) and (b) leading power factor of $\varphi_{pf} = +45°$ (*RC* load of 60 Ω + 50 μF).

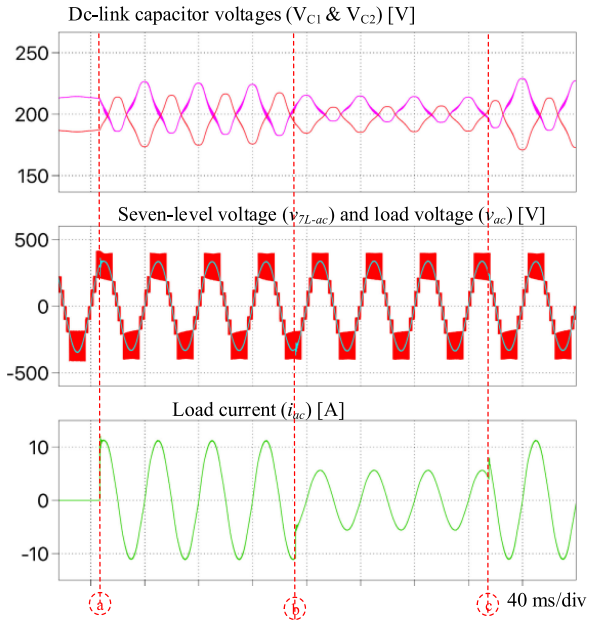

Fig. 15. Dynamic performance of the converter under several changes in the active power. (a) Step change in load from no load to full load (30 Ω). (b) Step change in load from full load (30 Ω) to half load (60 Ω). (c) Step change in load from half load (60 Ω) to full load (30 Ω).

be seen, the converter track their reference voltages very well under any load changes and confirms its good performance in both transient- and steady-state operations.

A conventional two-stage boost plus 7L-ANPC topology [see Fig. 2(c)] in a system similar to Fig. 4(a) and a single-stage system using 7L-ABNPC are simulated in PLECS in order to make a direct performance comparison. Parameters such as the

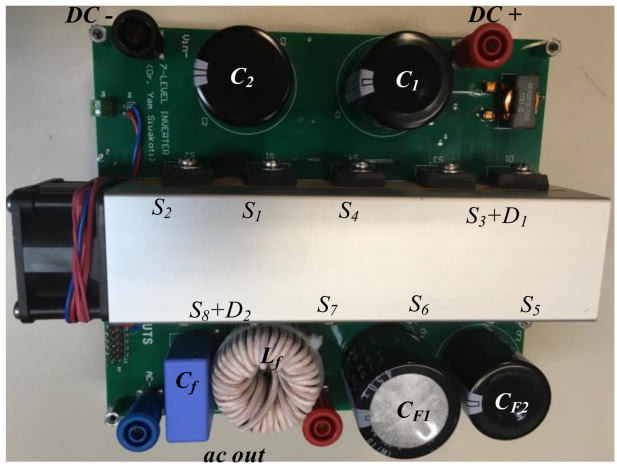

Fig. 16. Picture showing the prototype of a 2.2-kVA (single-phase) 7L inverter.

input voltage ($V_{\text{in}} = 400$ V), load (2.2 kVA), power factor ($\cos\varphi = 1$), switching frequency (15 kHz), modulation index ($M = 0.85$), and output voltage ($v_{\text{ac}} = 230$ V) are identical for both systems. The single-stage 7L-ABNPC demonstrates a 2%–3% higher efficiency over a wide range of loads. Using LS-PWM with feedforward control, the THD and dc-link capacitor voltage ripple is same for both topologies.

As a follow up, based on the satisfactory simulation results and to verify and validate the practicality of the proposed 7L inverter, a compact 2.2-kVA prototype was developed as shown in Fig. 16. All switches are 650-V SiC devices (SCT3022AL) from ROHM semiconductor. Experimental results under unity power-factor condition are shown from Figs. 17 to 21. Fig. 22 demonstrates the behavior of the inverter when operating in a

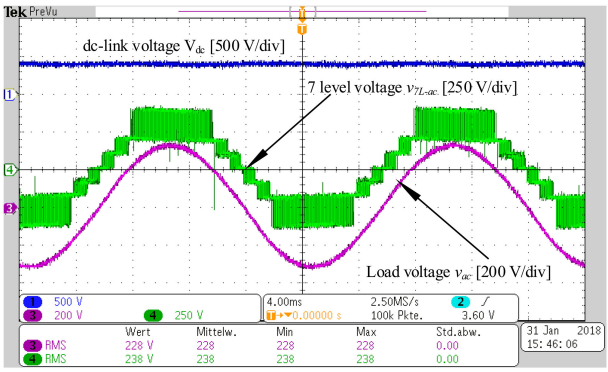

(a)

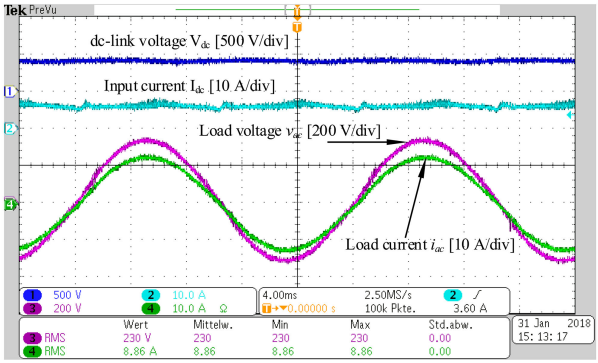

(b)

Fig. 17. Measured waveforms under unity power-factor condition showing inverter input/output voltage/current waveforms. The measured output current THD is 2.15%.

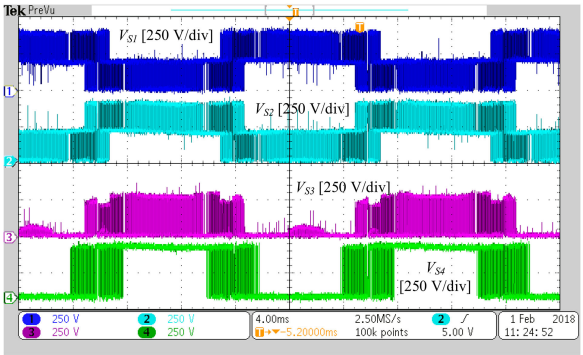

(a)

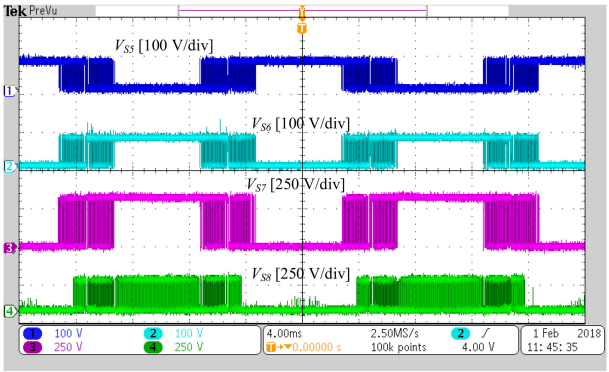

(b)

Fig. 18. Measured waveforms showing the voltage stress on the semiconductor devices.

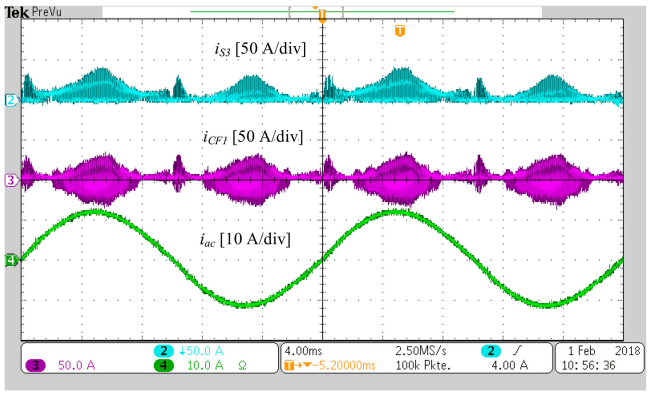

Fig. 19. Measured waveforms showing the current stress on C_{F1} and S_3 at full-load current.

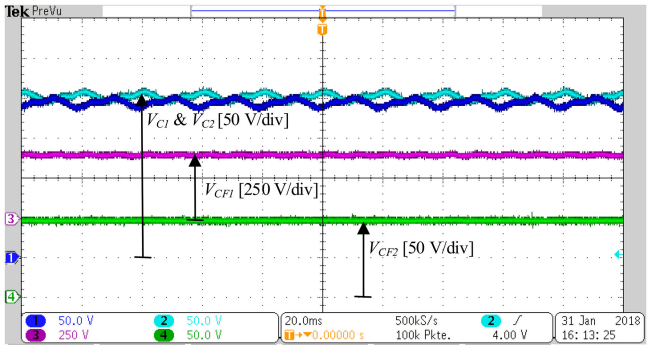

Fig. 20. Measured waveforms showing the input voltage, FC voltage, and upper and lower dc-link capacitor voltages.

reactive power mode. It can be seen that the inverter is capable of generating a 7L output voltage with a clean sinusoidal voltage and current.

Fig. 17(a) shows the inverter input/output voltage and current waveforms with clear 7Ls in the output voltage with a clear sinusoidal output voltage and current. Fig. 17(b) shows the input current of the inverter, which is continuous with a peak amplitude of around 5.5 A. Note that a dc-link voltage of 380 V (Ch. 1) magnitude is sufficient to achieve a line-neutral output voltage of 230 V_{RMS}. This is in contrast to conventional 7L topologies which would require a nominal dc link of close to 800 V. As shown in Fig. 18, the voltage stress on devices, respectively, corroborates the earlier analysis and simulation results. The peak current through S_{X3} and S_{X8} is ≈26 A as shown in Fig 19(b), which validates Fig. 13(c) and Table IV. Fig. 20 also shows the voltages of two dc-link capacitors and two FCs: Ch 1 is the upper dc-link capacitor voltage, Ch. 2 is the lower dc-link capacitor voltage, Ch. 3 is the C_{F1} voltage, and Ch. 4 is C_{F2} voltage. The measured peak-to-peak C_{F1} and C_{F2} voltage ripple is 10 V (= 10/400 V = 2.5%) and 2 V (= 2/100 V = 2%), respectively, and dc-link capacitor half-line-frequency voltage ripple is 22 V (= 22/200 V = 11%). The balanced FC and dc-link capacitor voltages verify the modulation method and confirm the advantage of the self-balancing in the proposed circuit. In addition, as shown in Fig. 21, the small *LC* output

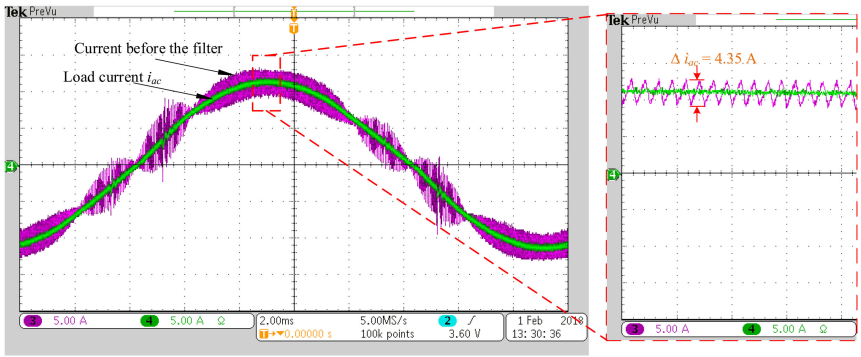

Fig. 21. Measured waveforms showing the inverter output currents (before and after the filter).

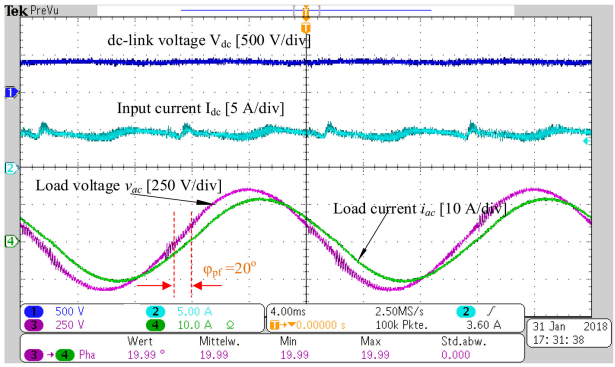

Fig. 22. Measured waveforms under reactive power condition ($\cos\varphi = 0.93$) showing inverter input/output voltage and current waveforms.

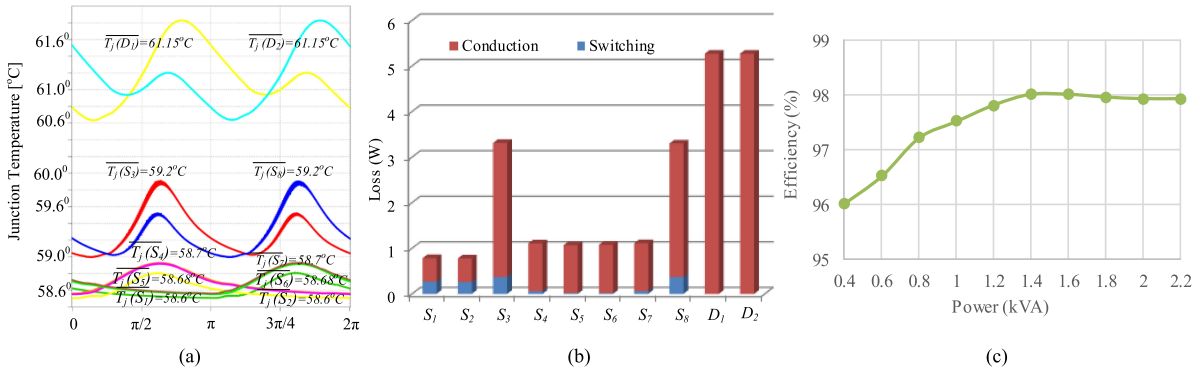

Fig. 23. (a) Steady-state operating junction temperature of the semiconductor. (b) Loss distribution. (c) Measured efficiency of the inverter.

filter provides good high-frequency attenuation and a maximum peak-to-peak current ripple amplitude of 4.35 A.

The reactive power operation mode is also tested as shown in Fig. 22 with power factor of 0.93 (inductive). The inverter still produces a good quality voltage and current waveform without high distortion (THD $< 1.8\%$).

The simulated averaged power loss distribution and the operating junction temperature (T_j) of the individual switching elements are presented in Fig. 23(a). A constant ambient temperature T_A of 40 °C is assumed in this analysis with uniform temperature distribution across the heat sink. As expected, the diodes and switches in the capacitor-charging path have higher loss (conduction), and, hence, relatively higher temperature $(\Delta\hat{T}_j \approx 3\ ^\circ\text{C})$ then the other switches. Fig. 23(b) shows similar findings and the loss distribution across the switching components. Fig. 23(c) shows the measured efficiency of the prototype inverter across a range of output power levels. The peak efficiency of the inverter is 98.2%.

VI. Conclusion

In this paper, a novel eight-switch 7L ANPC inverter is proposed. Modulation techniques are explored and operations under both active and reactive power-factor conditions are systemat-

ically analyzed. A comparative analysis and a set of design guidelines are presented and followed by simulation and experimental verification.

Compared to conventional 7L inverter topologies, the ANPC inverter topology requires only eight power devices for a single-phase design and halves the dc-link voltage required to produce a given ac voltage output magnitude when compared to similar circuits. For applications such as for a grid-connected PV system, this may help us to eliminate additional power conversion stages (boost converters), and, therefore, increase the efficiency and reliability of the system. Furthermore, this reduces the voltage stress on the dc-link capacitor, which reduces the cost and size of the system design. The inverter can operate at any power factor (leading or lagging) without requiring any changes to the modulation scheme.

Compared with other 7L configurations, the performance demonstrated by the new inverter is highly competitive, potentially making it an appropriate topology choice for a wide range of power conversion applications, e.g., variable-speed drives, electric vehicles (V2G/G2V technologies) and grid-connected renewable energy systems.

REFERENCES

[1] M. Schweizer, T. Friedli, and J. W. Kolar, "Comparative evaluation of advanced three-phase three-level inverter/converter topologies against two-level systems," *IEEE Trans. Ind. Electron.*, vol. 60, no. 12, pp. 5515–5527, Dec. 2012.

[2] H. Tian, Y. Li, and Y. W. Li, "A novel seven-level hybrid-clamped (HC) topology for medium voltage motor drives," *IEEE Trans. Power Electron.*, vol. 33, no. 7, pp. 5543–5547, Jul. 2018.

[3] S. Kouro *et al.*, "Recent advances and industrial applications of multilevel converters," *IEEE Trans. Ind. Electron.*, vol. 57, no. 8, pp. 2553–2580, Aug. 2010.

[4] J. Rodríguez, J. S. Lai, and F. Z. Peng, "Multilevel inverters: A survey of topologies, controls, and applications," *IEEE Trans. Ind. Electron.*, vol. 49, no. 4, pp. 724–738, Aug. 2002.

[5] J. I. Leon, S. Vazquez, and L. G. Franquelo, "Multilevel converters: Control and modulation techniques for their operation and industrial applications," *Proc. IEEE*, vol. 105, no. 11, pp. 2066–2081, Nov. 2017.

[6] J. Rodriguez, S. Bernet, P. K. Steimer, and I. E. Lizama, "A survey on neutral-point-clamped inverters," *IEEE Trans. Ind. Electron.*, vol. 57, no. 7, pp. 2219–2230, Jul. 2010.

[7] L. G. Franquelo, J. Rodriguez, J. I. Leon, S. Kouro, R. Portillo, and M. A. M. Prats, "The age of multilevel converters arrives," *IEEE Ind. Electron. Mag.*, vol. 2, no. 2, pp. 28–39, Jun. 2008.

[8] J. Rodríguez, S. Bernet, B. Wu, J. O. Pontt, and S. Kouro, "Multilevel voltage-source-converter topologies for industrial medium-voltage drives," *IEEE Trans. Ind. Electron.*, vol. 54, no. 6, pp. 2930–2945, Dec. 2007.

[9] X. Yuan, "Derivation of voltage source multilevel converter topologies," *IEEE Trans. Ind. Electron.*, vol. 64, no. 2, pp. 966–976, Feb. 2017.

[10] T. B. Soeriro, J. W. Kolar, P. Ranstad, and J. Linner, "Voltage source converter (VSC) with neutral-point-clamped (NPC) topology and method for operating such voltage source converter," U.S. Patent US20130272045A1, Oct. 17, 2017.

[11] C. Feng, J. Liang, and V. Agelidis, "Modified phase-shifted PWM control for flying capacitor multilevel converters," *IEEE Trans. Power Electron.*, vol. 22, no. 1, pp. 178–185, Jan. 2007.

[12] W. Sheng and Q. Ge, "A novel seven-level ANPC converter topology and its commutating strategies," *IEEE Trans. Power Electron.*, vol. 33, no. 9, pp. 7496–7509, Sep. 2018.

[13] F. Z. Peng, "A generalized multilevel inverter topology with self voltage balancing," *IEEE Trans. Ind. Appl.*, vol. 37, no. 2, pp. 611–618, Mar./Apr. 2001.

[14] M. Saeedifard, P. M. Barbosa, and P. K. Steimer, "Operation and control of a hybrid seven-level converter," *IEEE Trans. Power Electron.*, vol. 27, no. 2, pp. 652–660, Feb. 2012.

[15] S. R. Pulikanti, G. Konstantinou, and V. G. Agelidis, "Hybrid seven-level cascaded active neutral-point-clamped-based multilevel converter under SHE-PWM," *IEEE Trans. Ind. Electron.*, vol. 60, no. 11, pp. 4–17, Jan. 2015.

[16] M. A. Perez, S. Bernet, J. Rodriguez, S. Kouro, and R. Lizana, "Circuit topologies, modelling, control schemes, and applications of modular multilevel converters," *IEEE Trans. Power Electron.*, vol. 30, no. 1, pp. 652–660, Feb. 2012.

[17] P. Barbosa, P. Steimer, J. Steinke, M. Winkelnkemper, and N. Celanovic, "Active neutral-point-clamped (ANPC) multilevel converter technology," in *Proc. Eur. Conf. Power Electron. Appl.*, Sep. 2005, pp. 1–10.

[18] T. A. Meynard, H. Foch, P. Thomas, J. Courault, R. Jakob, and M. Nahrstaedt, "Multicell converters: Basic concepts and industry applications," *IEEE Trans. Ind. Electron.*, vol. 49, no. 5, pp. 955–964, Oct. 2002.

[19] A. Nabae, I. Takahashi, and H. Akagi, "A neutral-point-clamped PWM inverter," in *Proc. IEEE Ind. App. Soc. Annu. Meet. Conf. Rec.*, Oct. 1980, vol. 3, pp. 761–766.

[20] M. Manirekar, P. Steimer, and T. Lipo, "Hybrid multilevel power conversion system: A competitive solution for high-power applications," *IEEE Trans. Ind. Appl.*, vol. 36, no. 3, pp. 834–841, May 2000.

[21] T. Bruckner and S. Bemet, "Loss balancing in three-level voltage source inverters applying active NPC switches," in *Proc. IEEE 32nd Annu. Power Electron. Spec. Conf.*, Vancouver, BC, Canada, 2001, vol. 2, pp. 1135–1140.

[22] A. Chen and X. He, "Research on hybrid-clamped multilevel-inverter topologies," *IEEE Trans. Ind. Electron.*, vol. 53, no. 6, pp. 1898–1907, Dec. 2006.

[23] S. Mariethoz, "Systematic design of high-performance hybrid cascaded multilevel inverters with active voltage balance and minimum switching losses," *IEEE Trans. Power Electron.*, vol. 28, no. 7, pp. 3100–3113, Jul. 2013.

[24] Y. P. Siwakoti and F. Blaabjerg, "Common-ground-type transformerless inverters for single-phase solar photovoltaic systems," *IEEE Trans. Ind. Electron.*, vol. 65, no. 3, pp. 2100–2111, Mar. 2018.

Yam P. Siwakoti (S'10–M'14–SM'18) received the B.Tech. degree in electrical engineering from the National Institute of Technology, Hamirpur, India, in 2005, the M.E. degree in electrical power engineering from the Norwegian University of Science and Technology, Trondheim, Norway, and Kathmandu University, Dhulikhel, Nepal, in 2010, and the Ph.D. degree from Macquarie University, Sydney, N.S.W., Australia, in 2014.

He was a Postdoctoral Fellow with the Department of Energy Technology, Aalborg University, Denmark, from 2014 to 2016. He was a Visiting Scientist with the Fraunhofer Institute for Solar Energy Systems, Freiburg, Germany, from 2017 to 2018. He is currently a Lecturer with the Faculty of Engineering and Information Technology, University of Technology Sydney, Sydney, N.S.W., Australia.

Dr. Siwakoti was a Guest Associate Editor of the IEEE TRANSACTIONS ON POWER ELECTRONICS from 2015 to 2016. He is currently an Associate Editor of three major journals: the IEEE TRANSACTIONS ON POWER ELECTRONICS, the IEEE TRANSACTIONS ON INDUSTRIAL ELECTRONICS, and the *IET Power Electronics*. He is also a Peer-Review College Member of Engineering and Physical Science Research Council, U.K. He received the prestigious Green Talent Award from the Federal Ministry of Education and Research, Germany, in 2016.

Akshay Mahajan received the B.Tech. degree in electrical engineering from the College of Engineering Pune, Pune, India, in 2010, and the M.Sc. degree in electrical power engineering from the Technical University of Darmstadt, Darmstadt, Germany, 2014.

Since 2014, he has been a Research Assistant with Fraunhofer Institute of Solar Energy Systems ISE, Freiburg, Germany. His research interests include design of power converters for e-mobility applications and inductive power transfer.

Daniel J. Rogers (M'09) received the M.Eng. and Ph.D. degrees in electrical and electronic engineering from Imperial College London, London, U.K., in 2007 and 2011, respectively.

He is currently an Associate Professor with the Department of Engineering Science, University of Oxford, Oxford, U.K. He conducts research in collaboration with the industry and is an Investigator on U.K. EPSRC research projects in the areas of power electronics, grid-scale energy storage, microgrids, and HVdc transmission. His research interests include the use of medium- and large-scale power electronic systems to create flexible electrical networks that take the advantage of a diverse range of generation and storage technologies.

Frede Blaabjerg (S'86–M'88–SM'97–F'03) received the Ph.D. degree in electrical engineering from Aalborg University, Aalborg, Denmark, in 1992.

He was with ABB-Scandia, Randers, Denmark, from 1987 to 1988. He became an Assistant Professor in 1992, an Associate Professor in 1996, and a Full Professor of power electronics and drives in 1998 with Aalborg University. In 2017, he became a Villum Investigator. He is a Honoris Causa with the University Politehnica Timisoara, Timişoara, Romania and Tallinn Technical University, Tallinn, Estonia. He has published more than 600 journal papers in the fields of power electronics and its applications. He is the co-author of four monographs and editor of 10 books in power electronics and its applications. His current research interests include power electronics and its applications, such as in wind turbines, PV systems, reliability, harmonics, and adjustable-speed drives.

Dr. Blaabjerg received 30 IEEE Prize Paper Awards, the IEEE PELS Distinguished Service Award in 2009, the EPE-PEMC Council Award in 2010, the IEEE William E. Newell Power Electronics Award in 2014, and the Villum Kann Rasmussen Research Award in 2014. He was the Editor-in-Chief of the IEEE TRANSACTIONS ON POWER ELECTRONICS from 2006 to 2012. He has been a Distinguished Lecturer for the IEEE Power Electronics Society from 2005 to 2007 and for the IEEE Industry Applications Society from 2010 to 2011 as well as 2017 to 2018. In 2019 and 2020, he will serve as a President of the IEEE Power Electronics Society. He is the Vice-President of the Danish Academy of Technical Sciences. He was nominated from 2014 to 2018 as one of the 250 Most Cited Researchers in Engineering in the World by Thomson Reuters.